Supplementary Information for

Photosensitization Behavior of Ir(III) Complexes in Selective Reduction of CO_2 by Re(I)-Complex-Anchored TiO_2 Hybrid Catalyst

Ha-Yeon Cheong, So-Yoen Kim, Yang-Jin Cho, Dae Won Cho, Chul Hoon Kim, Ho-Jin Son,* Chyongjin Pac,* and Sang Ook Kang*

Department of Advanced Materials Chemistry, Korea University, Sejong 30019, Korea.

Sections	Titles	pages
	Detailed description of apparent quantum yield measurement	S2
Scheme S1.	Synthesis of heteroleptic Iridium(III) complexes.	S3
Figure S1	^{1}H NMR spectra of **Ir-CN**$^+$.	S4
Figure S2	^{13}C NMR spectra of **Ir-CN**$^+$.	S5
Figure S3	ESI-Mass spectra of **Ir-CN**$^+$.	S6
Figure S4	Molecular structure of **Ir-H**$^+$.	S7
Figure S5	Molecular structure of **Ir-OMe**$^+$.	S8
Table S1.	Crystal data and structure refinement for compound **Ir-H**$^+$ and **Ir-OMe**$^+$.	S9
Table S2.	Bond lengths [Å] and angles [°] for **Ir-H**$^+$.	S10
Table S3.	Bond lengths [Å] and angles [°] for **Ir-OMe**$^+$.	S11
Table S4.	Angles [deg] for **Ir-H**$^+$.	S12
Table S5	Angles [deg] for **Ir-OMe**$^+$.	S14
Figure S6	Absorption decay profile of PS in DMF containing 0.25 mM BIH after irradiation for 2 min.	S16
Table S6	Kinetic parameters of absorbance decay of PS$^{-\bullet}$ in DMF.	S17
Figure S7	Absorption spectra of **Ir-X**$^+$ in DMF containing 0.25 mM BIH after irradiation.	S18
Figure S8	Absorption spectra of Ru(bpy)$_3^{2+}$ in DMF containing 0.25 mM BIH after irradiation.	S19
Figure S9	Adsorption spectra change of catalyst solution after adsorption process of ReC with TiO_2 particles.	S20
Figure S10	Emission spectra of **Ir-X**$^+$ in 2-MeTHF at 77 K.	S21
Table S7	Phosphorescent Properties of **Ir-X**$^+$ in 2-MeTHF at 77 K.	S22
Figure S11	Absorption spectra of **Ir-H**$^+$, **Ir-OMe**$^+$ and **Ir-CN**$^+$ under long-term irradiation.	S23
Table S8	Results of visible light driven CO production with the binary PS–TiO_2/ReC catalyst in different conditions.	S24
Figure S12	Plots of CO formation versus time for PS–RePE in CO_2-purged DMF containing 0.1 M BIH.	S25
Figure S13	^{13}C NMR spectra in $^{13}CO_2$-saturated DMF-d_7/D_2O mixture solvent containing **Ir-^{t}Bu**$^+$ + TiO_2/ReC and 0.1 M BIH.	S26
Figure S14	GC spectrum of gas in the reaction vessel and MS spectra of each retention times.	S27
Figure S15	Stern−Volmer plot of the quenching experiment using PS and BIH in DMF.	S28
Table S9	Kinetic parameters of emission quenching of PS by BIH in DMF.	S29
Figure S16	Differential UV-vis absorption spectra obtained by flow electrolysis of **Ir-X**$^+$.	S30
Figure S17	Phosphorescence decay profiles of **Ir-^{t}Bu**$^+$–TiO_2/ReC and TiO_2 in DMF.	S31
Figure S18	Stern−Volmer plot of the quenching experiment using **Ir-^{t}Bu**$^+$ complex and RePE.	S32
Table S10	Kinetic parameters of quenching of **Ir-^{t}Bu**$^+$ by RePE in DMF.	S33
Figure S19	Normalized decay profiles of the absorption of [**Ir-^{t}Bu**$^+$]$^{-\bullet}$ and [**Ir-OMe**$^+$]$^{-\bullet}$ in the dark after 2 min irradiation.	S34
Figure S20	Normalized decay profiles of the absorption of [**Ir-H**$^+$]$^{-\bullet}$, [**Ir-Me**$^+$]$^{-\bullet}$ and [**Ir-^{t}Bu**$^+$]$^{-\bullet}$ in the dark after 30 s irradiation.	S35
Figure S21	Absorption spectra of **Ir-^{t}Bu**$^+$ + TiO_2 particles in DMF containing 0.25 mM BIH after irradiation.	S36
Figure S22	Absorbance change of Ru(bpy)$_3^{2+}$–TiO_2/ReC in DMF containing BIH and 2.5 vol% H_2O during photoreaction.	S37
Figure S23	Plot for the formation of CO and HCOOH versus irradiation time. **Ir-^{t}Bu**$^+$–TiO_2/ReC in CO_2-saturated DMF containing 0.1 M BIH.	S38
Figure S24	Plots of CO and formic acid formation versus time. Ru(bpy)$_3^{2+}$ + TiO_2/ReC in CO_2-saturated DMF containing 0.1 M BIH	S39
Table S11	Results of visible light driven CO production with the binary **Ir-^{t}Bu**$^+$–TiO_2/ReC catalyst in different conditions.	S40
Figure S25	Solution color change of **Ir-X**$^+$ in DMF containing 0.25 mM BIH after irradiation.	S41
Figure S26	Suspensions of **Ir-^{t}Bu**$^+$ + TiO_2 in DMF containing 0.25 mM BIH after irradiation for 1 h.	S42

Apparent Quantum yield measurement

$$\text{AQY} = \frac{2 \times \text{amount of } H_2 \text{ or CO generated per unit time}}{\text{number of incident photons per unit time}} \qquad \text{(eq. 1)}$$

The apparent quantum yield Φ(CO) for CO production was determined for the **Ir-OMe**$^{+}$–TiO_2/ReC and Dye/TiO_2/ReC suspensions, a band-pass filter (420−450 nm) was used to isolate the 436 nm light form the emission light of a high-pressure mercury lamp (1000 W, model 6171, Newport Corporation), and the incident light flux was determined by using a 0.2 M ferrioxalate actinometer solution.[1] The apparent quantum yield (AQY) of CO formation for the hybrid system in the presence of 2.5 vol% water was determined in a linear time–conversion region. As defined in eq 1, the measured AQY is not the real quantum yield with scientific definition but represents a relative estimate for the utilization efficiency of photogenerated electrons into CO formation with respect to the incident light intensity because the number of photons absorbed by the sensitizer cannot be exactly determined. The relatively low AQY appears to arise, at least in part, from poor light harvesting by the dye due to extensive light scattering in the particle dispersion system.

[1] A. M. Braun, M.-T. Maurette, E. Oliveros, *Photochemical Technology*; Wiley & Sons: New York, **1991**; pp 76−80 and references therein.

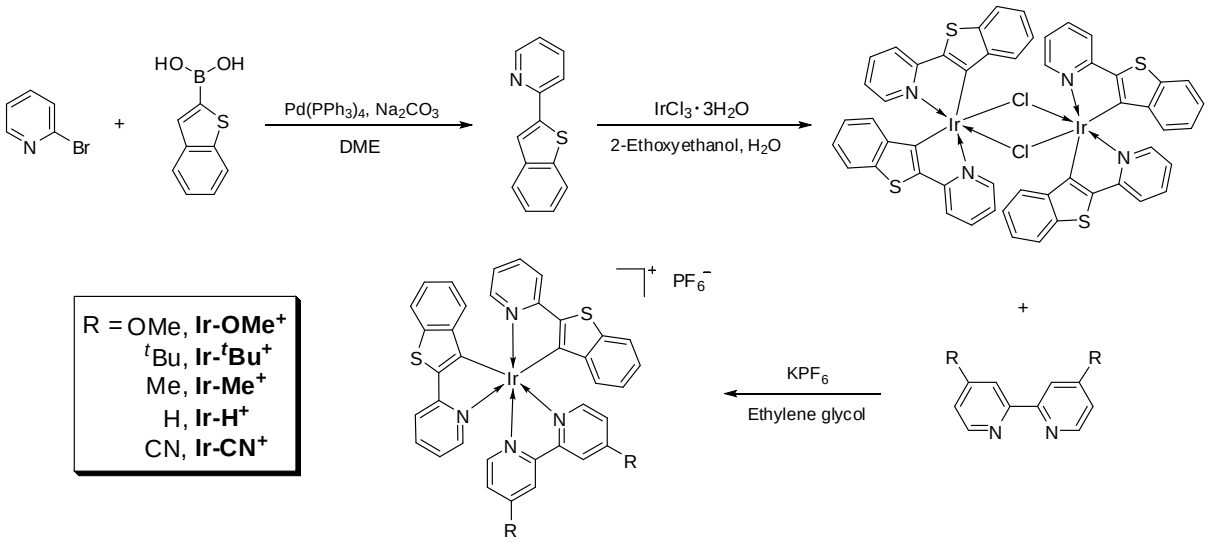

Scheme S1. Preparation of the **Ir-X**$^{+}$ sensitizers.

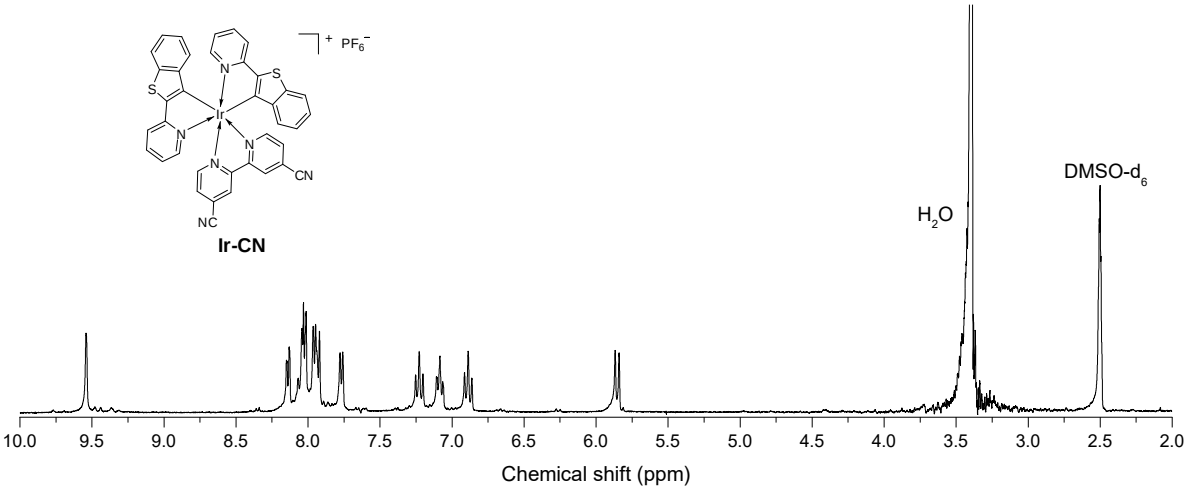

Figure S1. ^{1}H-NMR spectroscopic view of **Ir-CN**$^{+}$ in DMSO-d_6.

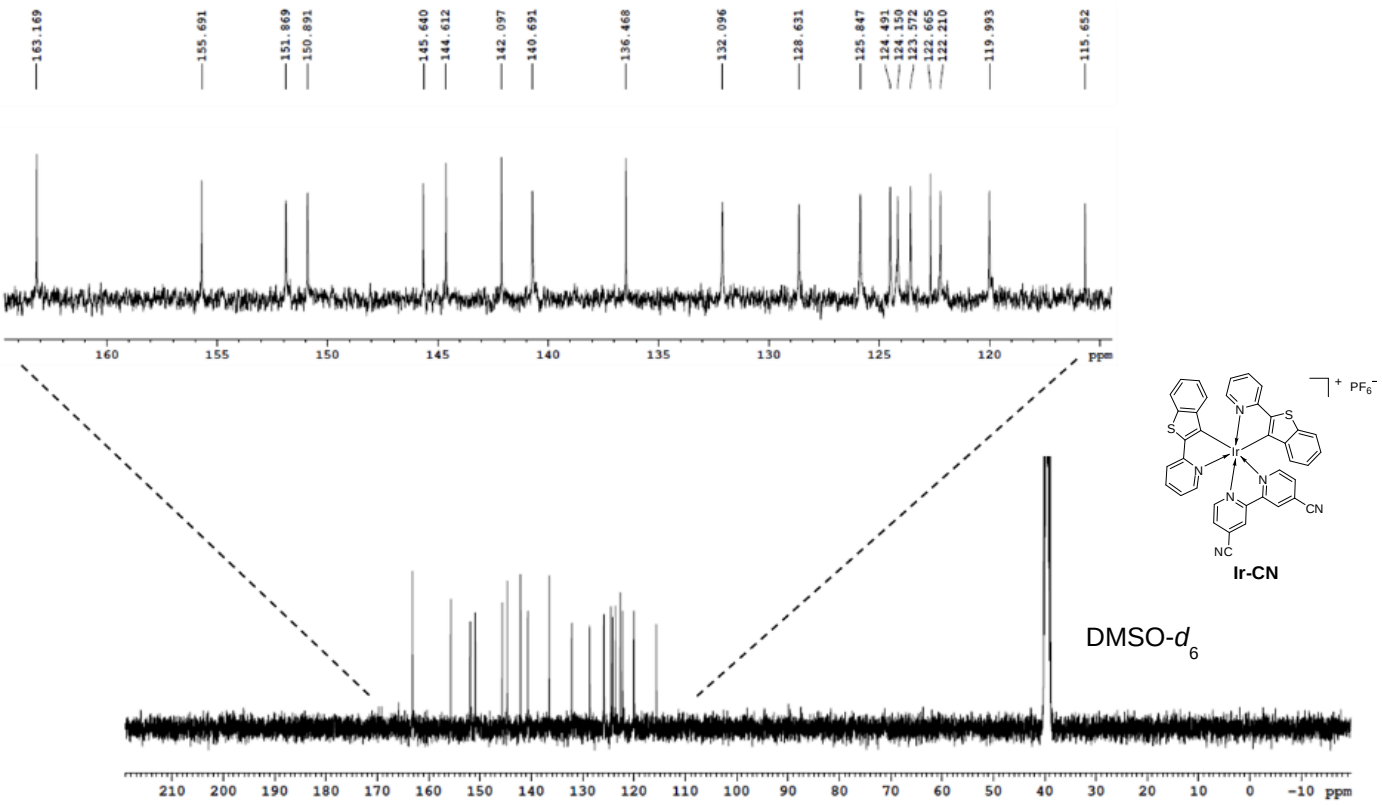

Figure S2. ^{13}C-NMR spectroscopic view of **Ir-CN**$^{+}$ in DMSO-d_6.

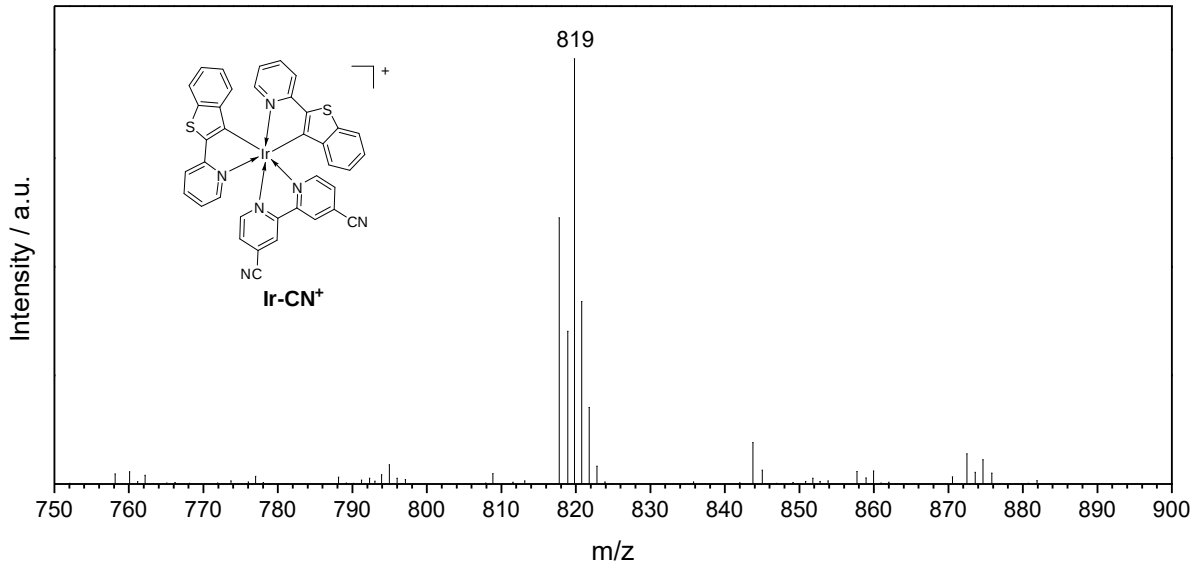

Figure S3. ESI-Mass spectra of **Ir-CN**$^{+}$.

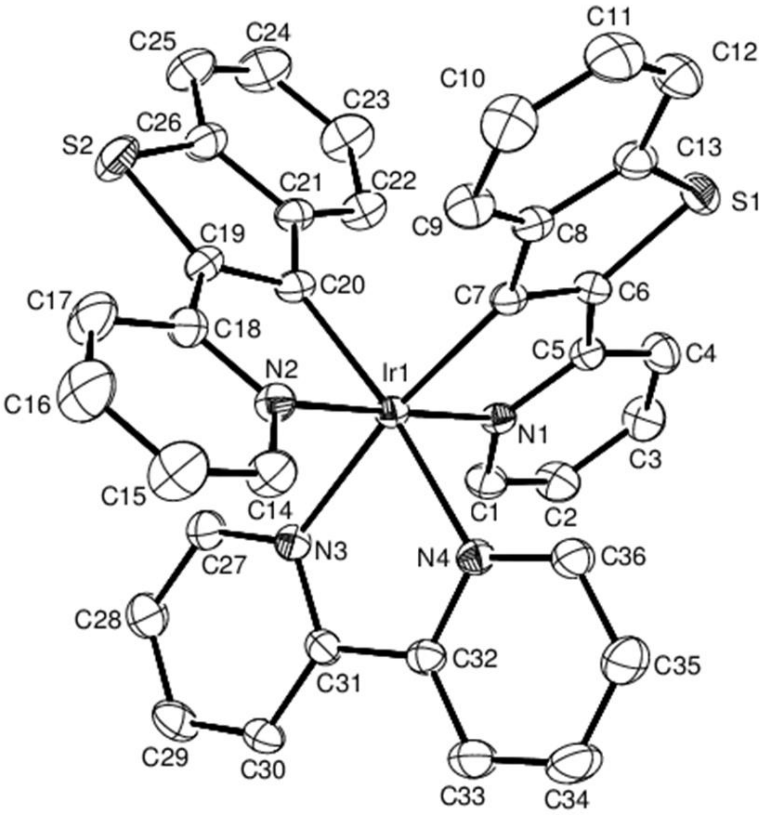

Figure S4. Molecular structure of **Ir-H**$^{+}$ with thermal ellipsoids drawn at the 30% level. Hydrogen atoms and PF_6 were omitted for clarity.

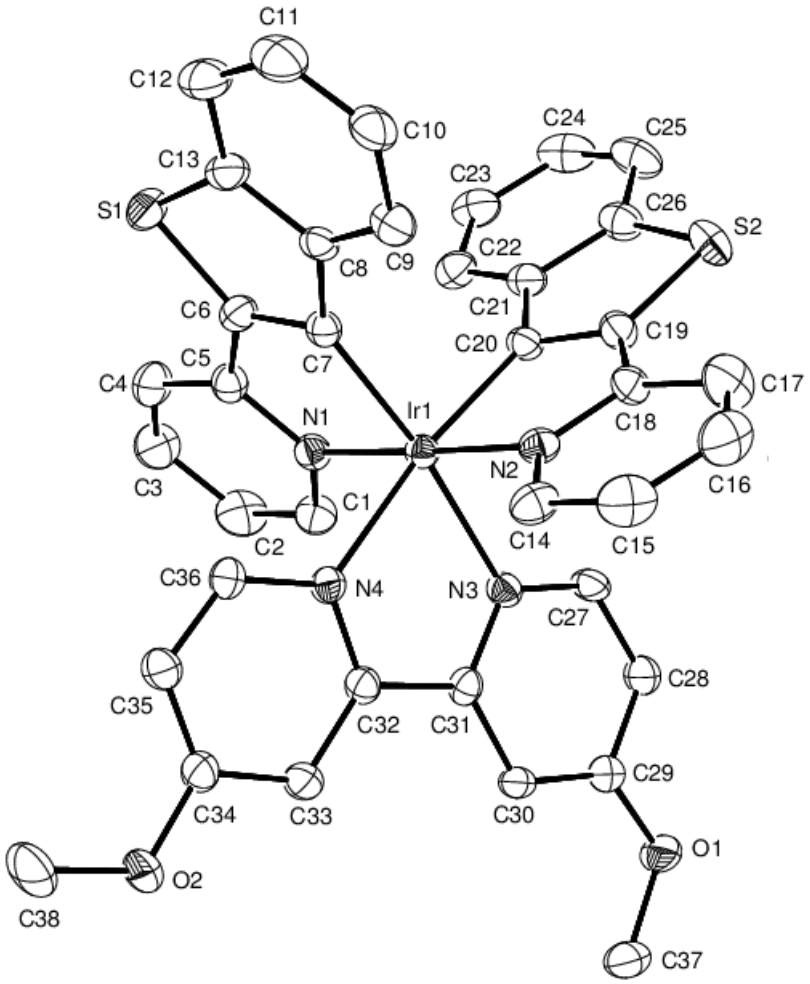

Figure S5. Molecular structure of **Ir-OMe**$^{+}$ with thermal ellipsoids drawn at the 30% level. Hydrogen atoms and PF_6 were omitted for clarity.

Table S1. Crystal data and structure refinement for **Ir-H**$^+$ and **Ir-OMe**$^+$.

Identification code	**Ir-H**$^+$	**Ir-OMe**$^+$
Empirical formula	$C_{36}H_{24}F_6IrN_4PS_2$	$C_{38}H_{28}F_6IrN_4O_2PS_2$
Formula weight	913.88	973.93
Temperature	293(2) K	293(2) K
Wavelength	0.71073 Å	0.71073 Å
Crystal system, space group	Monoclinic, $P2_1/n$	Monoclinic, $P2_1/c$
Unit cell dimensions	a = 10.493(7) Å	a = 14.718(3) Å
	b = 21.712(2) Å, β = 106.679(1)º	b = 14.518(3) Å, β= 108.159(3)º
	c = 17.753(1) Å	c = 19.673(3) Å
Volume	3874.3(4) Å^3	3994.3(1) Å^3
Z, D_{calc}	4, 1.567 g/cm^3	4, 1.620 g/cm^3
μ	3.654 mm^{-1}	3.553 mm^{-1}
F(000)	1784	1912
Crystal size	0.38 × 0.35 × 0.08 mm^3	0.20 × 0.18 × 0.08 mm^3
θ range for data collection	2.04 to 28.31º	1.46 to 28.38º
Limiting indices	$-13 \le h \le 13$, $-28 \le k \le 28$, $-23 \le l \le 23$	$-19 \le h \le 19$, $-19 \le k \le 19$, $-26 \le l \le 26$
Reflections collected / unique	52344 / 9627 [R_{int} = 0.0416]	53871 / 9962 [R_{int} = 0.0400]
Refinement method	Full-matrix least-squares on F^2	Full-matrix least-squares on F^2
Data / restraints / parameters	9627 / 0 / 451	9962 / 0 / 489
Goodness-of-fit on F^2	1.058	1.046
Final R indices [$I>2\sigma(I)$]	[a]R_1 = 0.0315, [b]wR_2 = 0.0785	[a]R_1 = 0.0286, [b]wR_2 = 0.0711
R indices (all data)	[a]R_1 = 0.0364, [b]wR_2 = 0.0804	[a]R_1 = 0.0396, [b]wR_2 = 0.0750
Largest diff. peak and hole	2.013 and –1.887 e.Å^{-3}	1.555 and –0.556 e.Å^{-3}

[a]$R_1 = \sum||F_o| - |F_c||$ (based on reflections with $F_o^2 > 2\sigma F^2$), [b]$wR_2 = [\sum[w(F_o^2 - F_c^2)^2]/\sum[w(F_o^2)^2]]^{1/2}$; $w = 1/[\sigma^2(F_o^2) + (0.095P)^2]$; $P = [\max(F_o^2, 0) + 2F_c^2]/3$(also with $F_o^2 > 2\sigma F^2$).

Table S2. Bond lengths [Å] for **Ir-H**$^{+}$.

Ir(1)-C(7)	2.026(3)	C(12)-C(13)	1.407(5)
Ir(1)-C(20)	2.029(3)	C(14)-C(15)	1.371(6)
Ir(1)-N(1)	2.059(3)	C(15)-C(16)	1.376(7)
Ir(1)-N(2)	2.065(3)	C(16)-C(17)	1.357(7)
Ir(1)-N(3)	2.118(3)	C(17)-C(18)	1.394(5)
Ir(1)-N(4)	2.119(3)	C(18)-C(19)	1.449(5)
S(1)-C(13)	1.734(4)	C(19)-C(20)	1.369(5)
S(1)-C(6)	1.747(3)	C(20)-C(21)	1.450(5)
S(2)-C(26)	1.739(5)	C(21)-C(22)	1.397(6)
S(2)-C(19)	1.741(4)	C(21)-C(26)	1.419(5)
N(1)-C(1)	1.348(4)	C(22)-C(23)	1.371(6)
N(1)-C(5)	1.364(4)	C(23)-C(24)	1.387(7)
N(2)-C(14)	1.344(5)	C(24)-C(25)	1.366(7)
N(2)-C(18)	1.357(5)	C(25)-C(26)	1.396(6)
N(3)-C(27)	1.341(5)	C(27)-C(28)	1.375(6)
N(3)-C(31)	1.357(4)	C(28)-C(29)	1.389(6)
N(4)-C(36)	1.332(5)	C(29)-C(30)	1.358(6)
N(4)-C(32)	1.361(4)	C(30)-C(31)	1.372(5)
C(1)-C(2)	1.362(5)	C(31)-C(32)	1.481(5)
C(2)-C(3)	1.374(6)	C(32)-C(33)	1.367(5)
C(3)-C(4)	1.380(6)	C(33)-C(34)	1.380(6)
C(4)-C(5)	1.391(5)	C(34)-C(35)	1.371(7)
C(5)-C(6)	1.438(5)	C(35)-C(36)	1.381(6)
C(6)-C(7)	1.376(5)	P(1)-F(2)	1.582(3)
C(7)-C(8)	1.438(5)	P(1)-F(6)	1.587(3)
C(8)-C(13)	1.410(5)	P(1)-F(3)	1.590(3)
C(8)-C(9)	1.413(5)	P(1)-F(1)	1.591(3)
C(9)-C(10)	1.373(6)	P(1)-F(4)	1.591(3)
C(10)-C(11)	1.395(7)	P(1)-F(5)	1.595(3)
C(11)-C(12)	1.364(7)		

Table S3. Bond lengths [Å] for **Ir-OMe**$^{+}$.

Ir(1)-C(20)	2.020(3)	C(10)-C(11)	1.387(6)
Ir(1)-C(7)	2.022(3)	C(11)-C(12)	1.378(6)
Ir(1)-N(1)	2.051(3)	C(12)-C(13)	1.393(5)
Ir(1)-N(2)	2.060(2)	C(14)-C(15)	1.387(5)
Ir(1)-N(4)	2.127(3)	C(15)-C(16)	1.390(6)
Ir(1)-N(3)	2.131(2)	C(16)-C(17)	1.354(6)
S(1)-C(6)	1.743(3)	C(17)-C(18)	1.406(5)
S(1)-C(13)	1.748(4)	C(18)-C(19)	1.424(4)
S(2)-C(26)	1.744(4)	C(19)-C(20)	1.379(5)
S(2)-C(19)	1.747(3)	C(20)-C(21)	1.443(4)
O(1)-C(29)	1.337(4)	C(21)-C(22)	1.401(5)
O(1)-C(37)	1.434(4)	C(21)-C(26)	1.411(5)
O(2)-C(34)	1.346(4)	C(22)-C(23)	1.373(5)
O(2)-C(38)	1.444(4)	C(23)-C(24)	1.404(6)
N(1)-C(1)	1.345(4)	C(24)-C(25)	1.347(6)
N(1)-C(5)	1.375(4)	C(25)-C(26)	1.395(5)
N(2)-C(18)	1.358(4)	C(27)-C(28)	1.374(4)
N(2)-C(14)	1.361(4)	C(28)-C(29)	1.381(4)
N(3)-C(27)	1.350(4)	C(29)-C(30)	1.383(4)
N(3)-C(31)	1.356(4)	C(30)-C(31)	1.383(4)
N(4)-C(36)	1.342(4)	C(31)-C(32)	1.482(4)
N(4)-C(32)	1.357(4)	C(32)-C(33)	1.380(4)
C(1)-C(2)	1.364(5)	C(33)-C(34)	1.402(4)
C(2)-C(3)	1.386(6)	C(34)-C(35)	1.371(5)
C(3)-C(4)	1.355(5)	C(35)-C(36)	1.375(4)
C(4)-C(5)	1.379(4)	P(1)-F(3)	1.559(3)
C(5)-C(6)	1.442(5)	P(1)-F(4)	1.563(3)
C(6)-C(7)	1.364(4)	P(1)-F(6)	1.564(3)
C(7)-C(8)	1.454(4)	P(1)-F(1)	1.577(3)
C(8)-C(9)	1.388(4)	P(1)-F(2)	1.585(3)
C(8)-C(13)	1.422(4)	P(1)-F(5)	1.590(3)
C(9)-C(10)	1.381(4)		

Table S4. Angles [deg] for **Ir-H**$^{+}$.

C(7)-Ir(1)-C(20)	89.7(1)	N(2)-C(14)-C(15)	122.1(4)
C(7)-Ir(1)-N(1)	80.2(1)	C(14)-C(15)-C(16)	119.1(4)
C(20)-Ir(1)-N(1)	98.7(1)	C(17)-C(16)-C(15)	119.9(4)
C(7)-Ir(1)-N(2)	100.3(1)	C(16)-C(17)-C(18)	119.1(4)
C(20)-Ir(1)-N(2)	79.9(1)	N(2)-C(18)-C(17)	121.2(4)
N(1)-Ir(1)-N(2)	178.4(1)	N(2)-C(18)-C(19)	112.2(3)
C(7)-Ir(1)-N(3)	171.6(1)	C(17)-C(18)-C(19)	126.6(4)
C(20)-Ir(1)-N(3)	97.1(1)	C(20)-C(19)-C(18)	119.2(3)
N(1)-Ir(1)-N(3)	93.8(1)	C(20)-C(19)-S(2)	115.9(3)
N(2)-Ir(1)-N(3)	85.9(1)	C(18)-C(19)-S(2)	124.9(3)
C(7)-Ir(1)-N(4)	96.1(1)	C(19)-C(20)-C(21)	109.9(3)
C(20)-Ir(1)-N(4)	172.3(1)	C(19)-C(20)-Ir(1)	112.7(3)
N(1)-Ir(1)-N(4)	87.4(1)	C(21)-C(20)-Ir(1)	137.4(3)
N(2)-Ir(1)-N(4)	94.1(1)	C(22)-C(21)-C(26)	117.2(4)
N(3)-Ir(1)-N(4)	77.6(1)	C(22)-C(21)-C(20)	130.6(3)
C(13)-S(1)-C(6)	89.4(2)	C(26)-C(21)-C(20)	112.2(3)
C(26)-S(2)-C(19)	89.6(2)	C(23)-C(22)-C(21)	120.4(4)
C(1)-N(1)-C(5)	118.4(3)	C(22)-C(23)-C(24)	121.1(5)
C(1)-N(1)-Ir(1)	125.8(2)	C(25)-C(24)-C(23)	120.9(4)
C(5)-N(1)-Ir(1)	115.9(2)	C(24)-C(25)-C(26)	118.4(4)
C(14)-N(2)-C(18)	118.5(3)	C(25)-C(26)-C(21)	121.9(4)
C(14)-N(2)-Ir(1)	125.4(3)	C(25)-C(26)-S(2)	125.7(3)
C(18)-N(2)-Ir(1)	115.8(2)	C(21)-C(26)-S(2)	112.4(3)
C(27)-N(3)-C(31)	118.4(3)	N(3)-C(27)-C(28)	122.9(4)
C(27)-N(3)-Ir(1)	125.8(3)	C(27)-C(28)-C(29)	118.3(4)
C(31)-N(3)-Ir(1)	115.8(2)	C(30)-C(29)-C(28)	118.7(4)
C(36)-N(4)-C(32)	119.0(3)	C(29)-C(30)-C(31)	121.1(4)
C(36)-N(4)-Ir(1)	125.5(2)	N(3)-C(31)-C(30)	120.6(3)
C(32)-N(4)-Ir(1)	115.5(2)	N(3)-C(31)-C(32)	115.5(3)
N(1)-C(1)-C(2)	122.4(4)	C(30)-C(31)-C(32)	123.9(3)
C(1)-C(2)-C(3)	119.9(4)	N(4)-C(32)-C(33)	120.7(4)
C(2)-C(3)-C(4)	118.8(4)	N(4)-C(32)-C(31)	115.7(3)

C(3)-C(4)-C(5)	119.4(4)	C(33)-C(32)-C(31)	123.5(3)
N(1)-C(5)-C(4)	121.0(3)	C(32)-C(33)-C(34)	120.2(4)
N(1)-C(5)-C(6)	112.0(3)	C(35)-C(34)-C(33)	118.7(4)
C(4)-C(5)-C(6)	127.0(3)	C(34)-C(35)-C(36)	119.0(4)
C(7)-C(6)-C(5)	119.6(3)	N(4)-C(36)-C(35)	122.3(4)
C(7)-C(6)-S(1)	115.6(3)	F(2)-P(1)-F(6)	90.4(2)
C(5)-C(6)-S(1)	124.7(3)	F(2)-P(1)-F(3)	90.8(2)
C(6)-C(7)-C(8)	109.4(3)	F(6)-P(1)-F(3)	89.7(2)
C(6)-C(7)-Ir(1)	112.4(2)	F(2)-P(1)-F(1)	89.5(2)
C(8)-C(7)-Ir(1)	138.2(3)	F(6)-P(1)-F(1)	90.8(2)
C(13)-C(8)-C(9)	117.0(3)	F(3)-P(1)-F(1)	179.4(2)
C(13)-C(8)-C(7)	113.1(3)	F(2)-P(1)-F(4)	179.4(3)
C(9)-C(8)-C(7)	129.9(4)	F(6)-P(1)-F(4)	90.0(2)
C(10)-C(9)-C(8)	120.4(4)	F(3)-P(1)-F(4)	88.9(2)
C(9)-C(10)-C(11)	121.0(5)	F(1)-P(1)-F(4)	90.9(2)
C(12)-C(11)-C(10)	121.1(4)	F(2)-P(1)-F(5)	90.0(2)
C(11)-C(12)-C(13)	118.1(4)	F(6)-P(1)-F(5)	179.5(2)
C(12)-C(13)-C(8)	122.4(4)	F(3)-P(1)-F(5)	90.5(2)
C(12)-C(13)-S(1)	125.1(3)	F(1)-P(1)-F(5)	89.0(2)
C(8)-C(13)-S(1)	112.5(3)	F(4)-P(1)-F(5)	89.5(2)

Symmetry transformations used to generate equivalent atoms.

Table S5. Angles [deg] for **Ir-OMe**$^{+}$.

C(20)-Ir(1)-C(7)	89.2(1)	C(14)-C(15)-C(16)	118.9(3)
C(20)-Ir(1)-N(1)	99.0(1)	C(17)-C(16)-C(15)	119.9(3)
C(7)-Ir(1)-N(1)	80.1(1)	C(16)-C(17)-C(18)	120.1(4)
C(20)-Ir(1)-N(2)	79.8(1)	N(2)-C(18)-C(17)	120.2(3)
C(7)-Ir(1)-N(2)	98.8(1)	N(2)-C(18)-C(19)	112.5(3)
N(1)-Ir(1)-N(2)	178.4(9)	C(17)-C(18)-C(19)	127.3(3)
C(20)-Ir(1)-N(4)	172.5(1)	C(20)-C(19)-C(18)	119.3(3)
C(7)-Ir(1)-N(4)	98.1(1)	C(20)-C(19)-S(2)	114.9(2)
N(1)-Ir(1)-N(4)	84.3(1)	C(18)-C(19)-S(2)	125.8(2)
N(2)-Ir(1)-N(4)	97.0(1)	C(19)-C(20)-C(21)	110.3(3)
C(20)-Ir(1)-N(3)	96.5(1)	C(19)-C(20)-Ir(1)	112.4(2)
C(7)-Ir(1)-N(3)	172.8(1)	C(21)-C(20)-Ir(1)	137.3(2)
N(1)-Ir(1)-N(3)	94.7(1)	C(22)-C(21)-C(26)	117.3(3)
N(2)-Ir(1)-N(3)	86.5(1)	C(22)-C(21)-C(20)	130.0(3)
N(4)-Ir(1)-N(3)	76.4(9)	C(26)-C(21)-C(20)	112.7(3)
C(6)-S(1)-C(13)	89.4(2)	C(23)-C(22)-C(21)	120.4(4)
C(26)-S(2)-C(19)	89.9(2)	C(22)-C(23)-C(24)	120.2(4)
C(29)-O(1)-C(37)	118.7(3)	C(25)-C(24)-C(23)	121.5(4)
C(34)-O(2)-C(38)	117.5(3)	C(24)-C(25)-C(26)	118.4(4)
C(1)-N(1)-C(5)	118.3(3)	C(25)-C(26)-C(21)	122.2(4)
C(1)-N(1)-Ir(1)	125.9(2)	C(25)-C(26)-S(2)	125.6(3)
C(5)-N(1)-Ir(1)	115.8(2)	C(21)-C(26)-S(2)	112.2(2)
C(18)-N(2)-C(14)	119.4(3)	N(3)-C(27)-C(28)	122.5(3)
C(18)-N(2)-Ir(1)	115.5(2)	C(27)-C(28)-C(29)	119.6(3)
C(14)-N(2)-Ir(1)	125.0(2)	O(1)-C(29)-C(28)	115.9(3)
C(27)-N(3)-C(31)	117.7(3)	O(1)-C(29)-C(30)	125.3(3)
C(27)-N(3)-Ir(1)	125.3(2)	C(28)-C(29)-C(30)	118.8(3)
C(31)-N(3)-Ir(1)	116.9(2)	C(31)-C(30)-C(29)	118.9(3)
C(36)-N(4)-C(32)	117.5(3)	N(3)-C(31)-C(30)	122.5(3)
C(36)-N(4)-Ir(1)	125.5(2)	N(3)-C(31)-C(32)	114.4(3)
C(32)-N(4)-Ir(1)	116.4(2)	C(30)-C(31)-C(32)	123.1(3)
N(1)-C(1)-C(2)	122.7(3)	N(4)-C(32)-C(33)	122.2(3)

C(1)-C(2)-C(3)	118.9(3)	N(4)-C(32)-C(31)	115.5(2)
C(4)-C(3)-C(2)	119.3(4)	C(33)-C(32)-C(31)	122.3(3)
C(3)-C(4)-C(5)	120.6(4)	C(32)-C(33)-C(34)	118.6(3)
N(1)-C(5)-C(4)	120.3(3)	O(2)-C(34)-C(35)	125.5(3)
N(1)-C(5)-C(6)	111.6(3)	O(2)-C(34)-C(33)	115.1(3)
C(4)-C(5)-C(6)	128.1(3)	C(35)-C(34)-C(33)	119.4(3)
C(7)-C(6)-C(5)	119.4(3)	C(34)-C(35)-C(36)	118.4(3)
C(7)-C(6)-S(1)	116.3(2)	N(4)-C(36)-C(35)	123.8(3)
C(5)-C(6)-S(1)	124.3(2)	F(3)-P(1)-F(4)	91.3(2)
C(6)-C(7)-C(8)	109.8(3)	F(3)-P(1)-F(6)	90.2(2)
C(6)-C(7)-Ir(1)	112.9(2)	F(4)-P(1)-F(6)	90.3(2)
C(8)-C(7)-Ir(1)	137.3(2)	F(3)-P(1)-F(1)	178.8(2)
C(9)-C(8)-C(13)	117.5(3)	F(4)-P(1)-F(1)	89.5(3)
C(9)-C(8)-C(7)	130.2(3)	F(6)-P(1)-F(1)	90.7(2)
C(13)-C(8)-C(7)	112.3(3)	F(3)-P(1)-F(2)	88.7(2)
C(10)-C(9)-C(8)	120.6(3)	F(4)-P(1)-F(2)	179.1(2)
C(9)-C(10)-C(11)	121.1(4)	F(6)-P(1)-F(2)	90.6(2)
C(12)-C(11)-C(10)	120.4(4)	F(1)-P(1)-F(2)	90.5(2)
C(11)-C(12)-C(13)	118.7(4)	F(3)-P(1)-F(5)	90.4(2)
C(12)-C(13)-C(8)	121.8(3)	F(4)-P(1)-F(5)	90.8(2)
C(12)-C(13)-S(1)	126.1(3)	F(6)-P(1)-F(5)	178.7(2)
C(8)-C(13)-S(1)	112.1(3)	F(1)-P(1)-F(5)	88.7(2)
N(2)-C(14)-C(15)	121.4(3)	F(2)-P(1)-F(5)	88.3(2)

Symmetry transformations used to generate equivalent atoms.

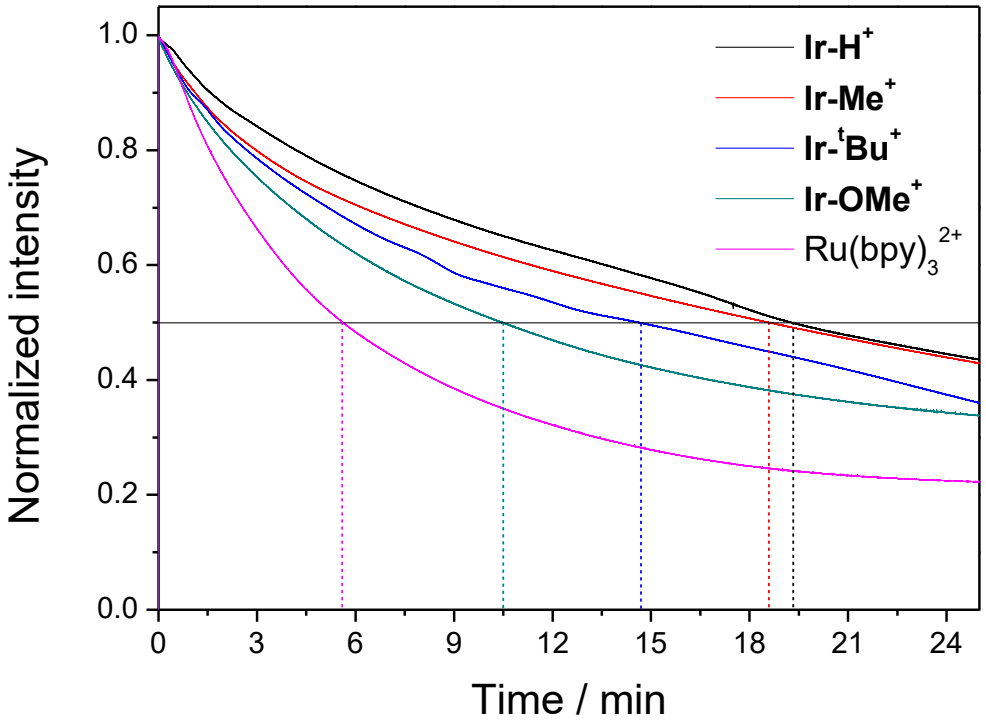

Figure S6. Normalized decay profiles of the absorption at 529 ± 15 nm (λ_{max} of $PS^{-\bullet}$) in the dark after 2 min irradiation for 3 mL Ar-saturated DMF/H_2O mixture solvent (2.5 vol% water) containing 0.025 mM PS and 2.5 mM BIH.

Table S6. Kinetic parameters of absorbance decay of $PS^{-\bullet}$ in DMF.[a]

Sensitizer	$t_{1/2}$ (min)[b]
Ir-H$^+$	19.5
Ir-Me$^+$	18.5
Ir-^{t}Bu$^+$	14.5
Ir-OMe$^+$	10.5
$Ru(bpy)_3^{2+}$	5.5

[a]Reaction condition: BIH (2.5 mM) + PS (0.025 mM) in an Ar-saturated DMF/H_2O mixture solvent (2.5 vol% water). [b]Half life time of $PS^{-\bullet}$ absorbance decay (at λ = 529 ± 15 nm).

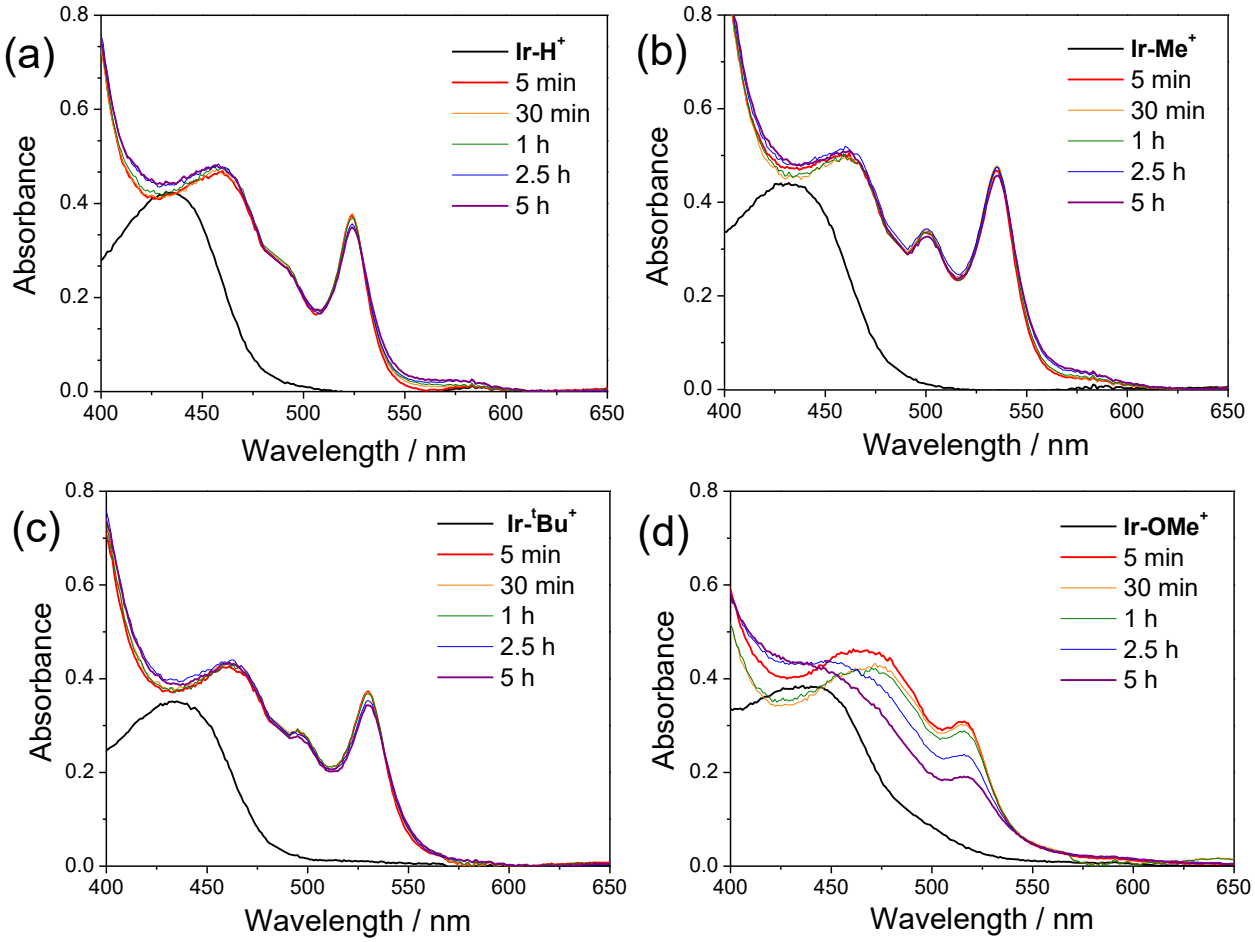

Figure S7. Changes of absorption spectra of (a) **Ir-H**$^+$, (b) **Ir-Me**$^+$, (c) **Ir-**^{t}**Bu**$^+$, and (d) **Ir-OMe**$^+$ following irradiation time (0–5 h) for Ar-saturated DMF containing 0.05 mM **Ir-X**$^+$ and 0.25 mM BIH; LED irradiation at >400 nm.

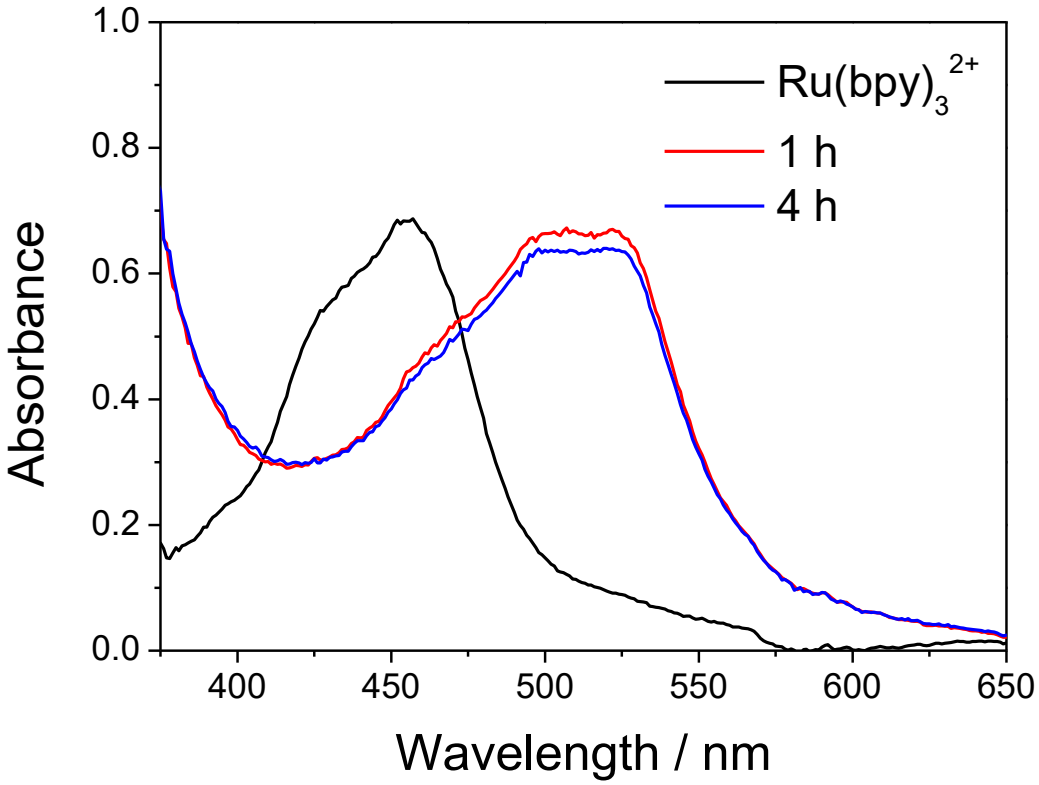

Figure S8. Changes of absorption spectra of $Ru(bpy)_3^{2+}$ following irradiation time (0–4 h) for DMF containing 0.25 mM BIH; LED irradiation at >400 nm.

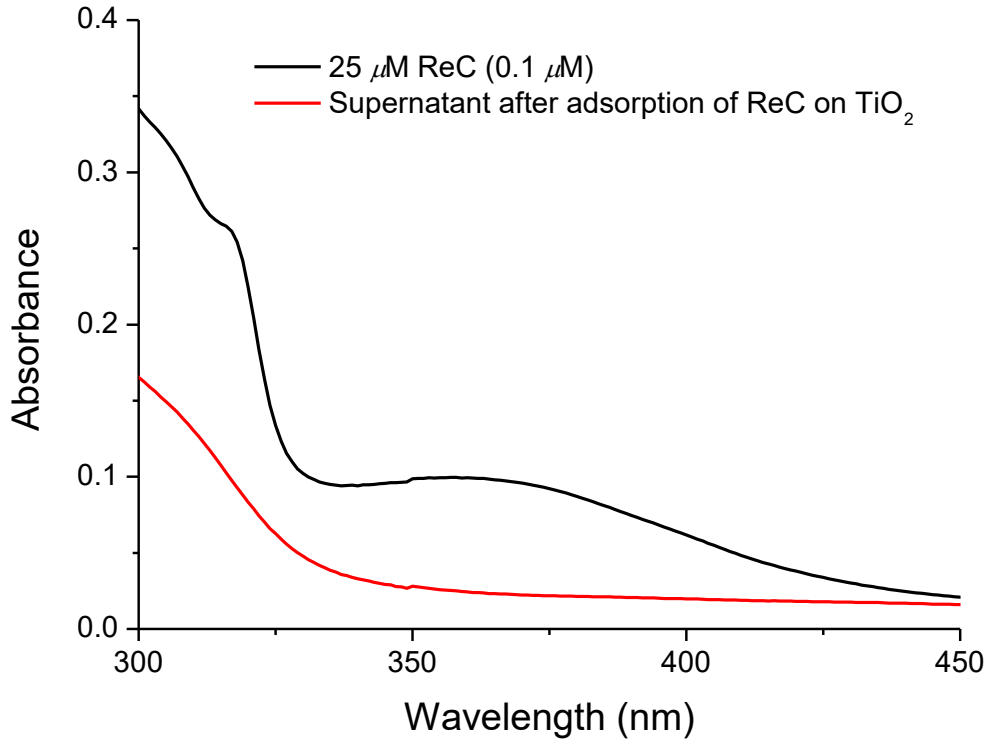

Figure S9. Comparison of adsorption spectra of catalyst solution before and after adsorption process of ReC with TiO_2 particles. The almost complete drop of absorbance means successful adsorption of added catalysts. Therefore, we think that the amount of ReC used in adsorption process is equivalent to the content of catalyst fixed on the TiO_2 particles (10 μmol/g, ReC/TiO_2).

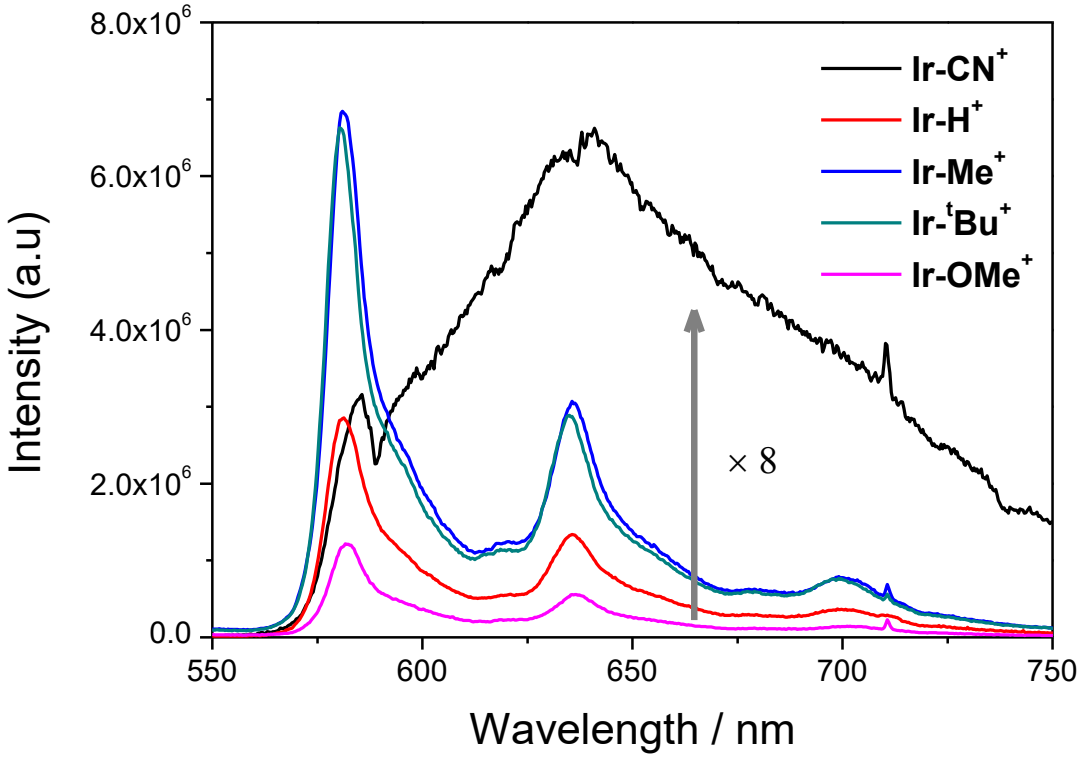

Figure S10. Emission spectra of **Ir-X**$^{+}$ (10 μM) taken by excitation at 416 nm in 2-MeTHF at 77 K.

Table S7. Phosphorescent Properties of **Ir-X**$^+$ in 2-MeTHF at 77 K.

	λ_{em} (nm)[a]	E_{0-0} (eV)[b]
Ir-OMe$^+$	581, 636, 701	2.13
Ir-^{t}**Bu**$^+$	580, 635. 699	2.13
Ir-Me$^+$	581, 635, 699	2.13
Ir-H$^+$	581, 635, 699	2.13
Ir-CN$^+$	585, 641	2.12

[a]Phosphorescence maxima. [b]Triplet energy is obtained from following equation: $E_{0-0} = 1240/\lambda_{max}$ of phosphorescent emission.

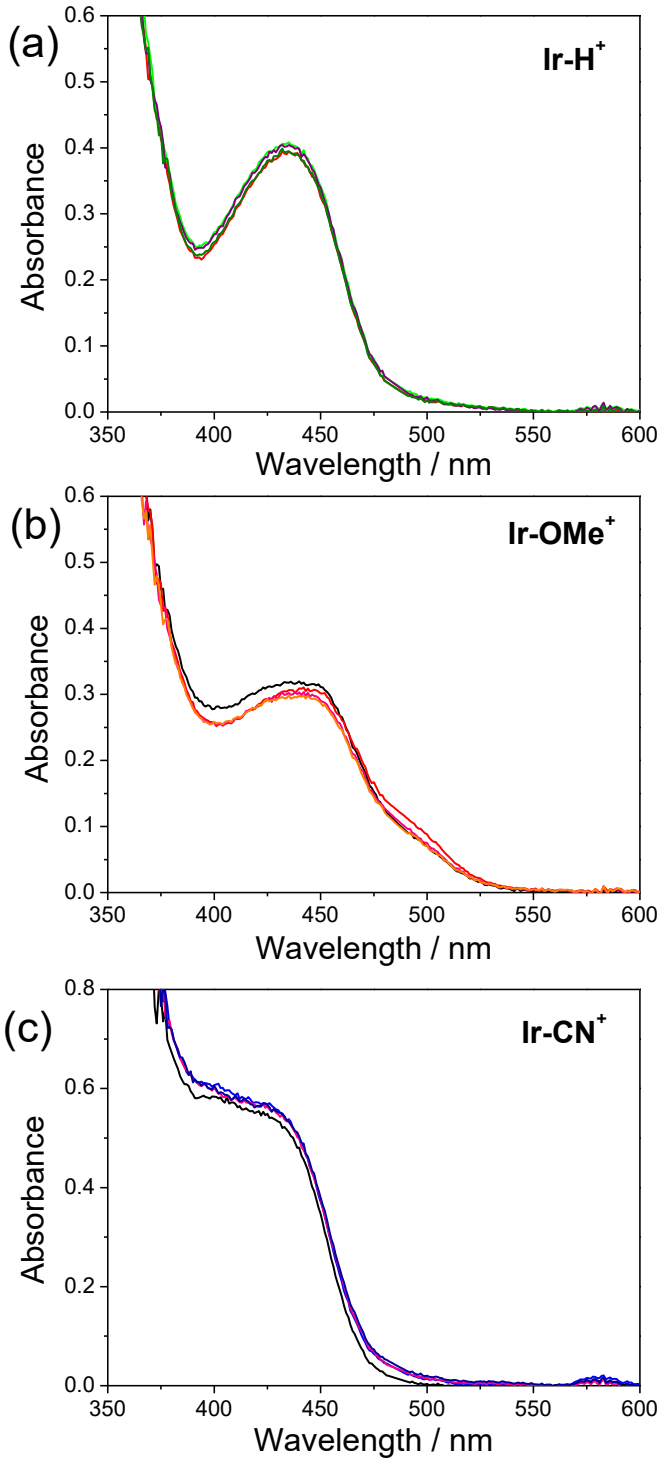

Figure S11. Changes of absorption spectra of (a) **Ir-H**$^+$ (50 μM), (b) **Ir-OMe**$^+$ (50 μM), and (c) **Ir-CN**$^+$ (50 μM) in DMF during 24 h LED irradiation.

Table S8. Results of visible light driven CO production with the binary PS + TiO_2/ReC catalyst in different conditions.[a]

System	PS	*n* PS / μmol	*n* ReC / μmol	Amount of CO produced @4 h		AQY / CO[b]
				TON	μmol	
PS–TiO_2/ReC	**Ir-OMe$^+$**	3	0.1	187 ± 15	18.7 ± 1.5	(3.7 ± 0.2) × 10^{-2}
	Ir-^{t}Bu$^+$			147 ± 9	14.7 ± 0.9	
	Ir-Me$^+$			137 ± 10	13.7 ± 1.0	-
	Ir-H$^+$			124 ± 10	12.4 ± 1.0	-
	Ir-CN$^+$			71 ± 5	7.1 ± 0.5	-
	$Ru(bpy)_3^{2+}$			61 ± 7	6.1 ± 0.7	-
w/o BIH	**Ir-^{t}Bu$^+$**			*n.d.*[c]	*n.d.*[c]	
PS–RePE	**Ir-OMe$^+$**	1.5	1.5	37 ± 3	55.6 ± 4.5	-
	Ir-^{t}Bu$^+$			29 ± 2	43.5 ± 3	-
	Ir-Me$^+$			32 ± 2.5	48.1 ± 3.75	-
	Ir-H$^+$			27 ± 2	40.5 ± 3	-
	Ir-CN$^+$			19 ± 2	28.6 ± 3	-
	$Ru(bpy)_3^{2+}$			23 ± 1.8	34.4 ± 2.7	-
Dye/TiO_2/ReC		1.5	0.1	106	10.6	(1.8 ± 0.3) × 10^{-2}
TiO_2/ReC	-	-	0.1	~2	~0.2	-

[a]All photocatalytic reactions were performed in CO_2-saturated DMF/H_2O mixture solvent (2.5 vol% water) containing 0.1 M BIH. [b]AQY (apparent quantum yield) = 2 × amount of CO generated per unit time / number of incident photons per unit time. [c]Not detected.

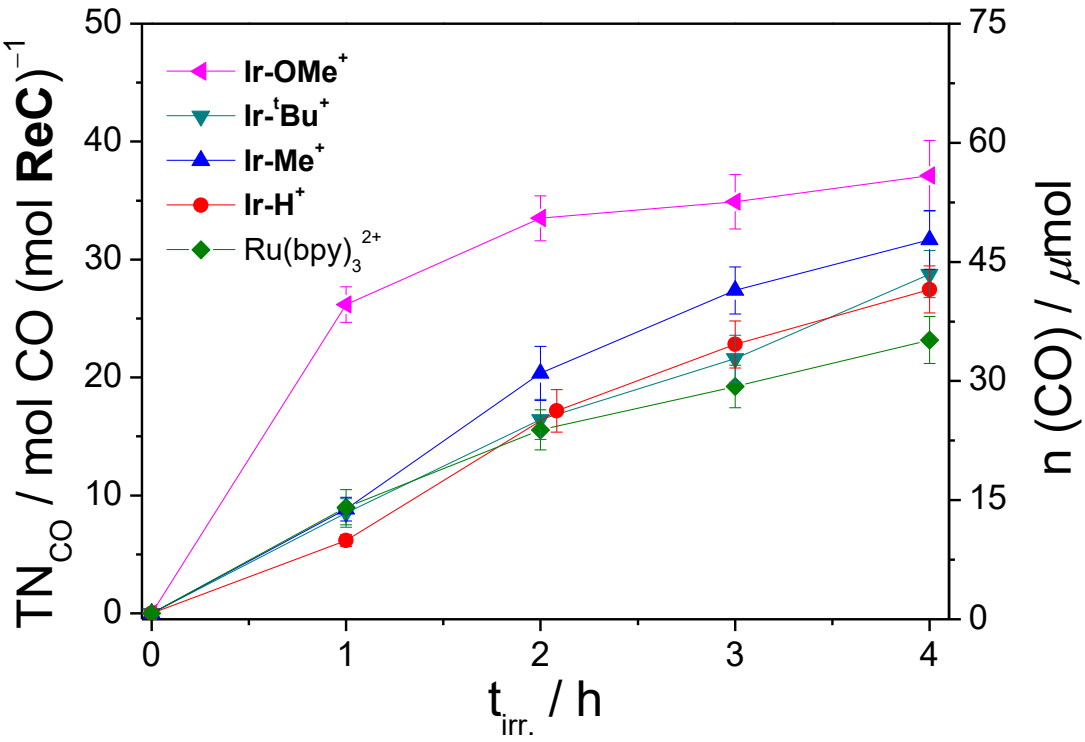

Figure S12. Plots of CO formation versus time for PS (0.5 mM) + RePE (0.5 mM) in 3 mL CO_2-saturated DMF containing 0.1 M BIH; irradiation at >400 nm.

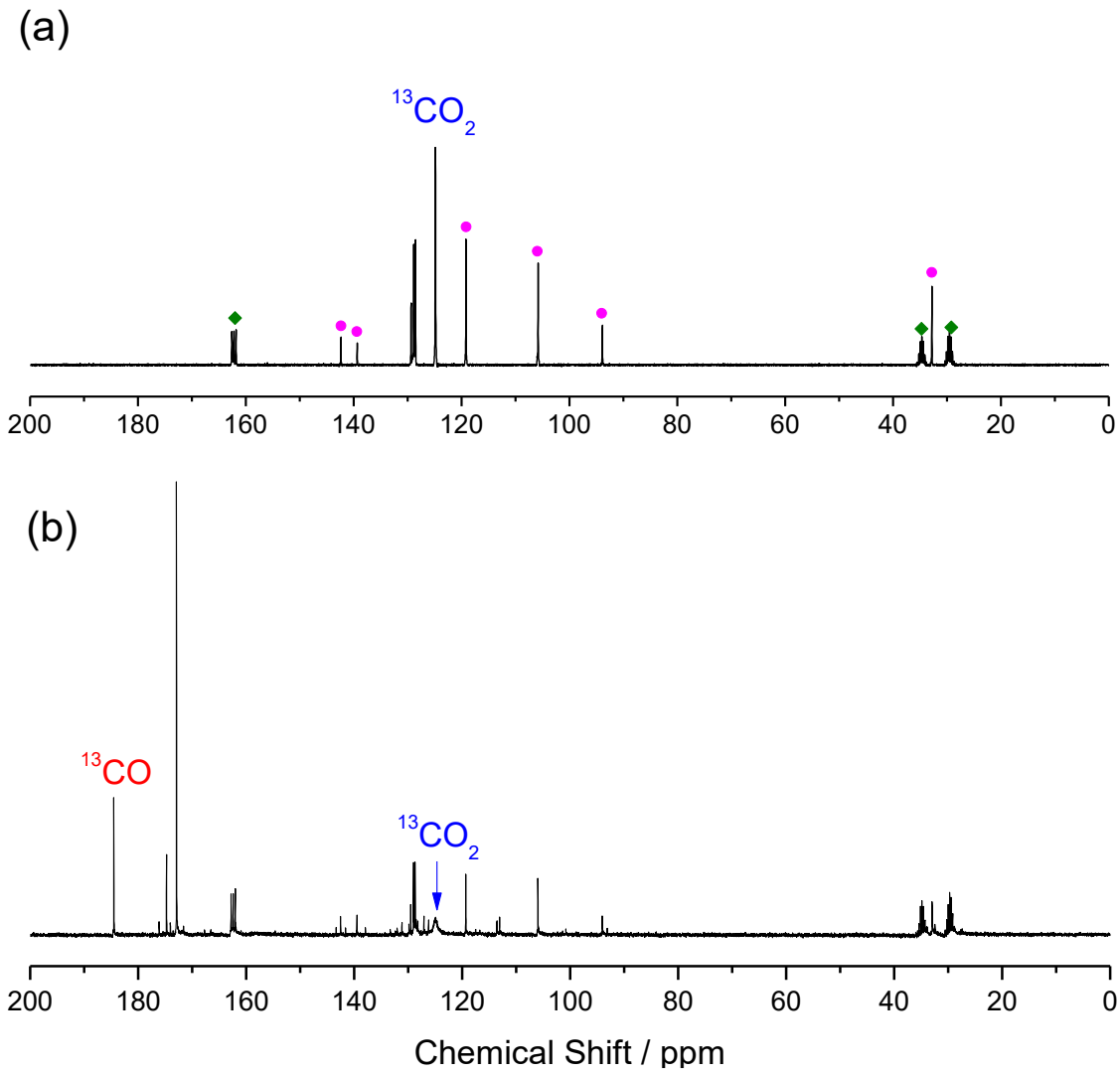

Figure S13. ^{13}C NMR spectra before (a) and after (b) irradiation in $^{13}CO_2$-saturated DMF-d_7/D_2O mixture solvent (2.5 vol% D_2O) containing **Ir-^{t}Bu$^+$** (1.5 mM) + TiO_2/ReC (15 mg) dispersion and 0.1 M BIH; irradiation at >400 nm. The symbols ◆ and ● represent the peaks of DMF and BIH, respectively.

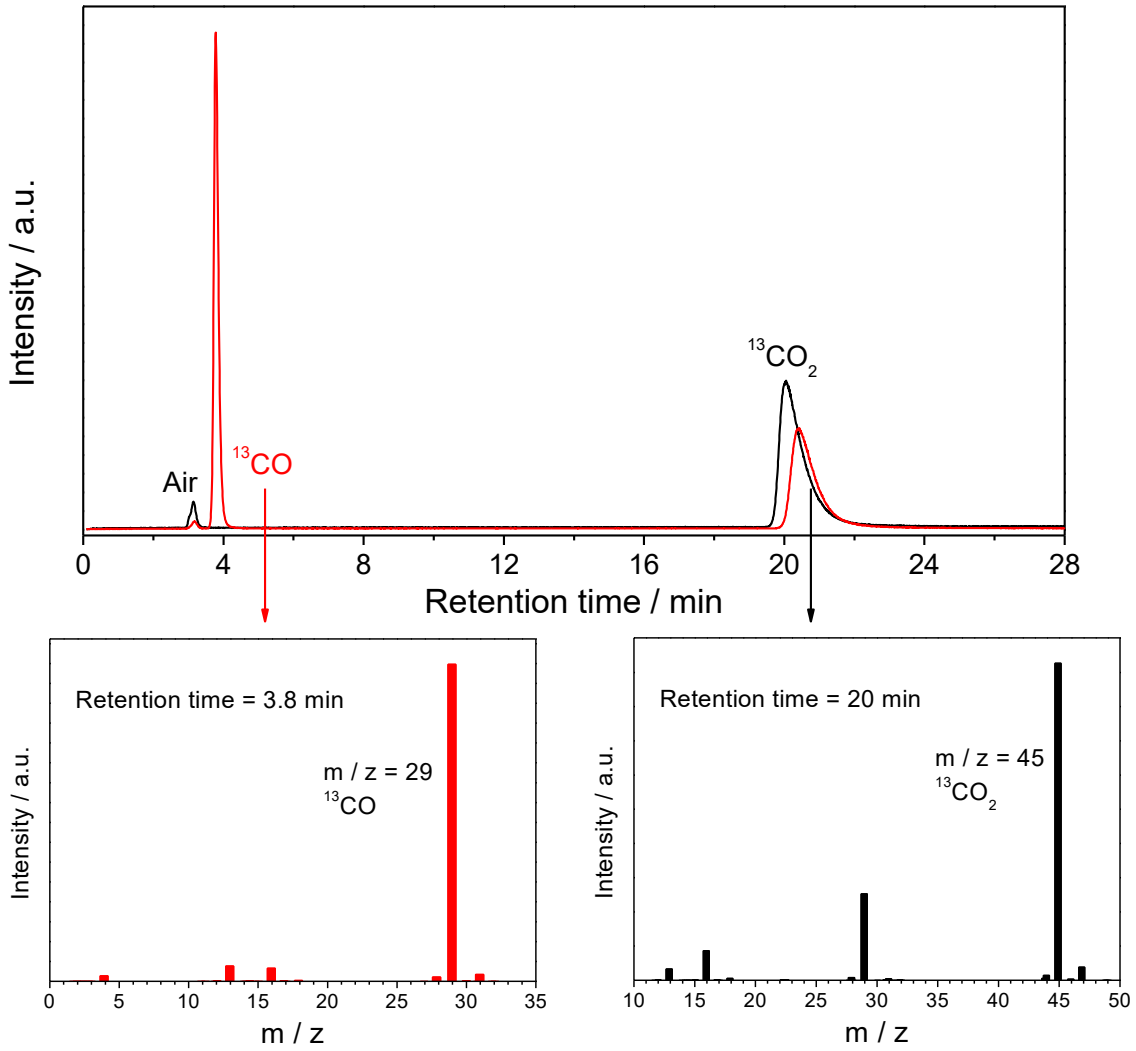

Figure S14. GC spectrum of gas in the reaction vessel before irradiation (black line), after irradiation (red line), and MS spectra of each retention times: GC-MS spectra was measured by Agilent Technologies 7890A GC equipped with 5975C inert MSD with Triple-Axis detector using a SUPELCO CarboxenTM 1010 PLOT Fused Silica Capillary column.

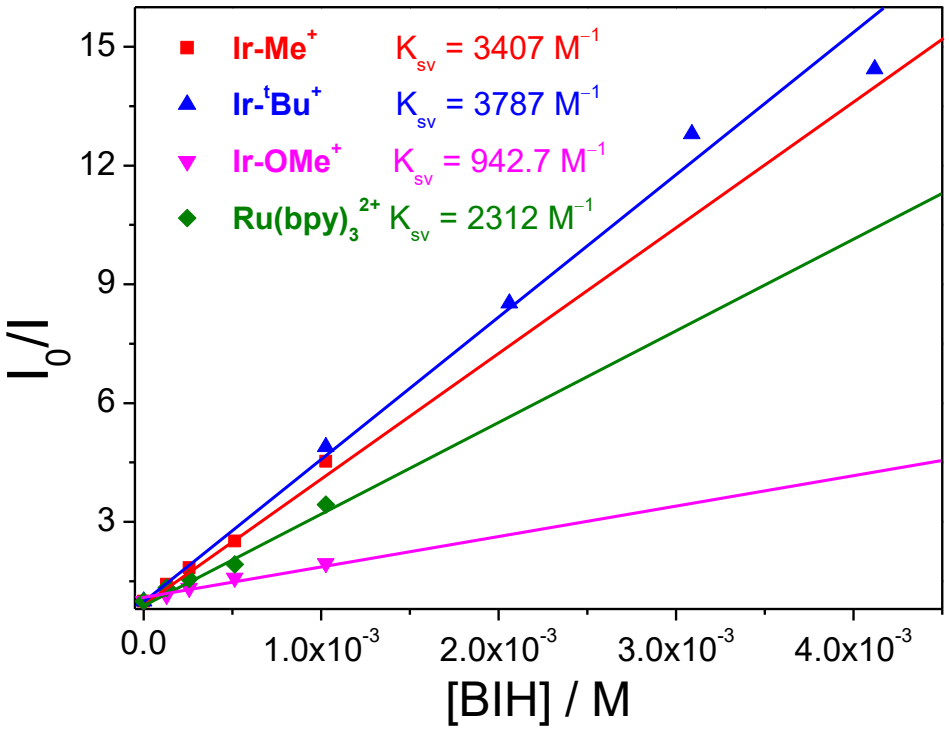

Figure S15. Stern−Volmer plot for emission quenching (at 578 nm for **Ir-X**$^{+}$ and 620 nm for $Ru(bpy)_3^{2+}$) of PS by BIH in DMF at 298 K; λ_{ex} = 434 ± 20 nm.

Table S9. Kinetic parameters of emission quenching of PS by BIH in DMF.[a]

Sensitizer	K_{sv} (M^{-1})[b]	t (μs)[c]	k_q (10^8 M^{-1} s^{-1})[d]
Ir-Me$^+$	3407	4.39	7.76
Ir-^{t}Bu$^+$	3787	6.47	5.85
Ir-OMe$^+$	942.7	5.64	1.67
$Ru(bpy)_3^{2+}$	2312	0.855	27

[a]Reaction condition: BIH + PS (0.23 mM) in DMF, λ_{ex} = 434 ± 20 nm. [b]Stern−Volmer quenching constant. [c]Phosphorescence lifetime of the PS measured in an Ar-saturated DMF without the quencher. [d]Quenching rate constant calculated using $k_q = K_{SV}/\tau_0$.

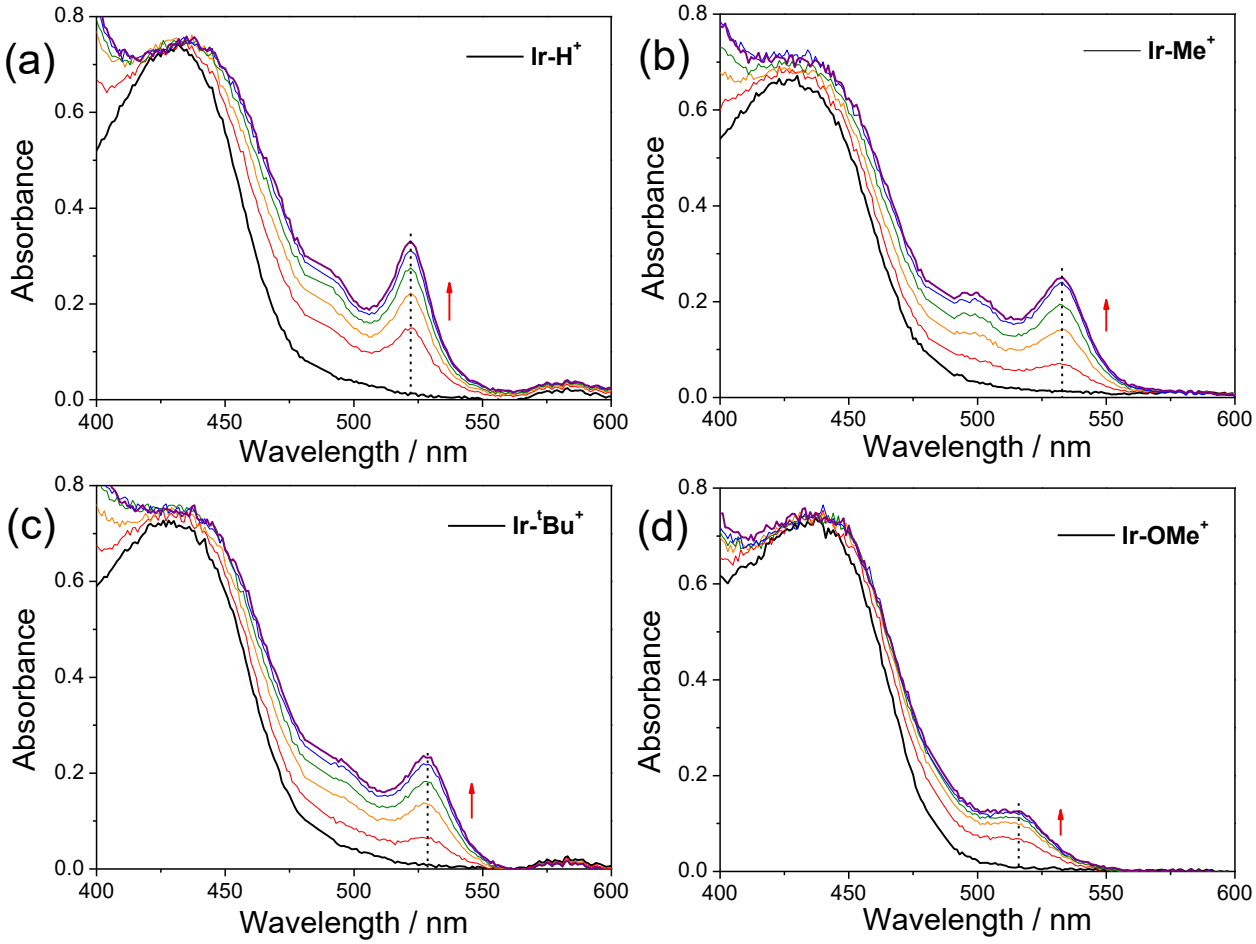

Figure S16. Differential UV-vis absorption spectra obtained by flow electrolysis of (a) **Ir-H**$^+$ (1 mM), (b) **Ir-Me**$^+$ (1 mM), (c) **Ir-**^{t}**Bu**$^+$ (1 mM), and (d) **Ir-OMe**$^+$ (1 mM) in an Ar-saturated acetonitrile containing 0.1 M TBAP with a Pt mesh working electrode. The changes of absorption peaks for [**Ir-X**$^+$]$^{-\bullet}$ generated was measured, at a fixed potential (−1.6 V vs. Ag/$AgNO_3$), at different times (an interval of ~10 s).

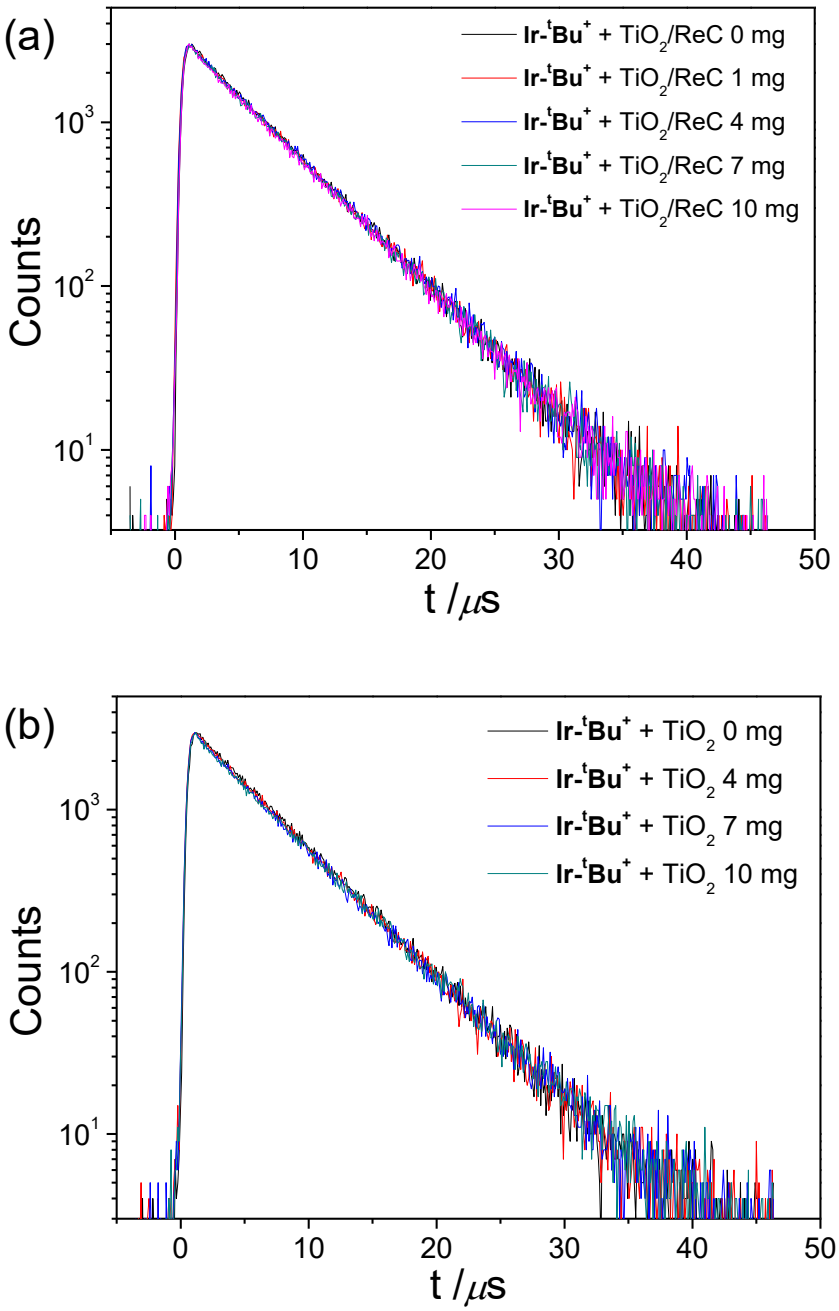

Figure S17. Phosphorescence decay profiles of **Ir-^{t}Bu$^+$** in the presence of either TiO_2/ReC (a) or TiO_2 (b) in DMF at room temperature: the amount of TiO_2/ReC or TiO_2 particles = 0 mg, 1 mg, 4 mg, 7 mg, and 10 mg. The dispersed TiO_2 particles were continuously stirred during measurement. These results indicate that the oxidative quenching pathway is not dominant in these binary systems; λ_{ex} = 430 nm.

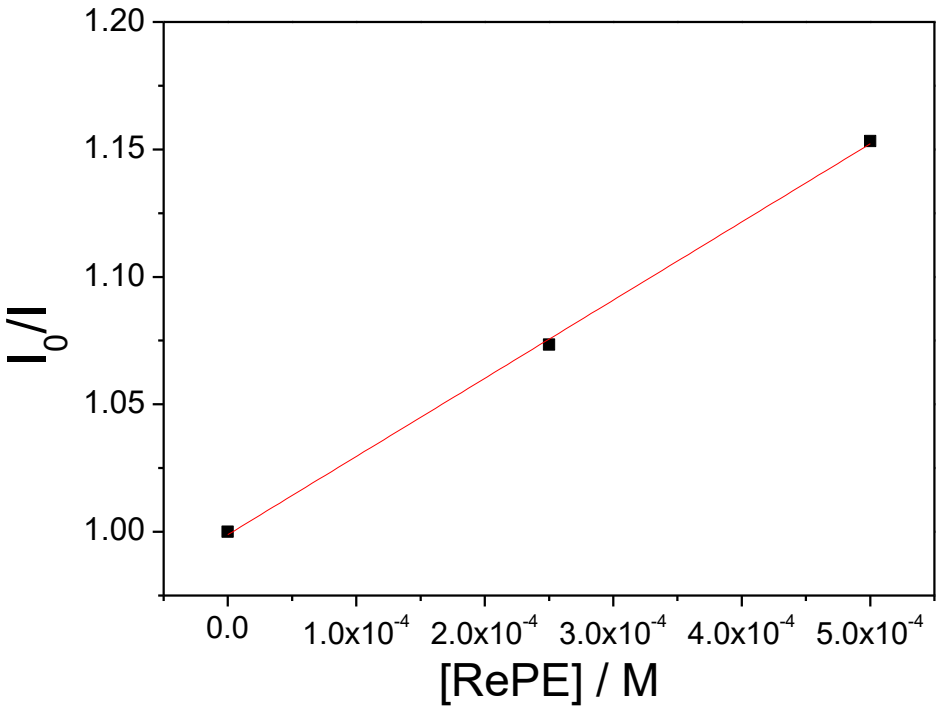

Figure S18. Stern−Volmer plot for emission quenching (at 578 nm (λ_{max})) of **Ir-^{t}Bu$^+$** complex (0.2 mM) by RePE in DMF at 298 K; λ_{ex} = 430 nm.

Table S10. Kinetic parameters of quenching by RePE in DMF.[a]

Sensitizer	K_{sv} (M^{-1})[b]	t (μs)[c]	k_q (10^6 M^{-1} s^{-1})[d]
Ir-^{t}Bu$^+$	306	6.47	4.7

[a]Reaction condition: RePE + **Ir-^{t}Bu$^+$** (0.2 mM) in DMF, λ_{ex} = 430 nm. [b]Stern−Volmer quenching constant. [c]Phosphorescence lifetime of the PS measured in deaerated without the quencher. [d]Quenching rate constant calculated using $k_q = K_{SV}/\tau_0$.

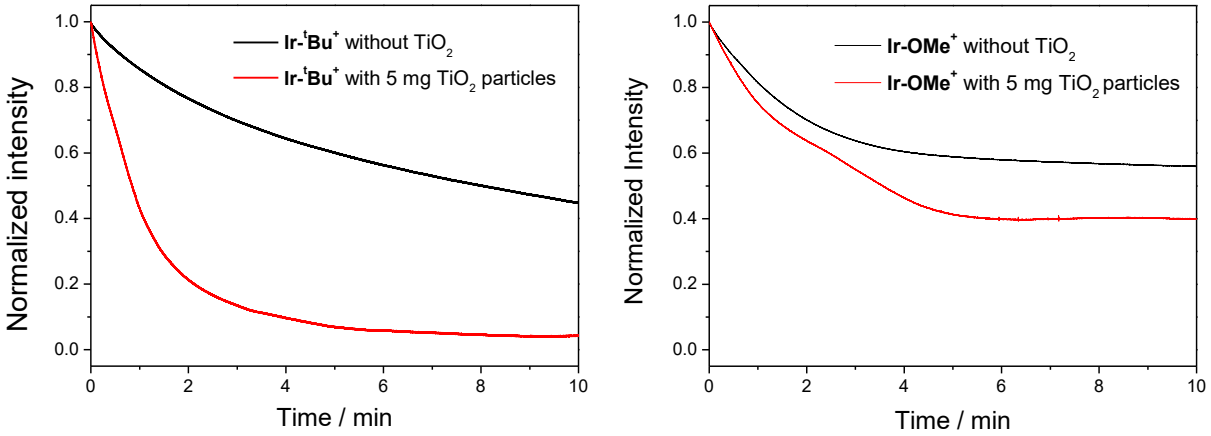

Figure 19. Normalized decay profiles of the absorption at 529 nm (λ_{max} of [**Ir-^{t}Bu**$^+$]$^{-\bullet}$, left) and 516 nm (λ_{max} of [**Ir-OMe**$^+$]$^{-\bullet}$, right) in the dark after 2 min irradiation of 3 mL DMF solution of 25 μM **Ir-X**$^+$, 2.5 mM BIH, and 2.5 vol% H_2O in the absence of TiO_2 (black line), with 5 mg TiO_2 particles placed in the bottom of the cell (red line).

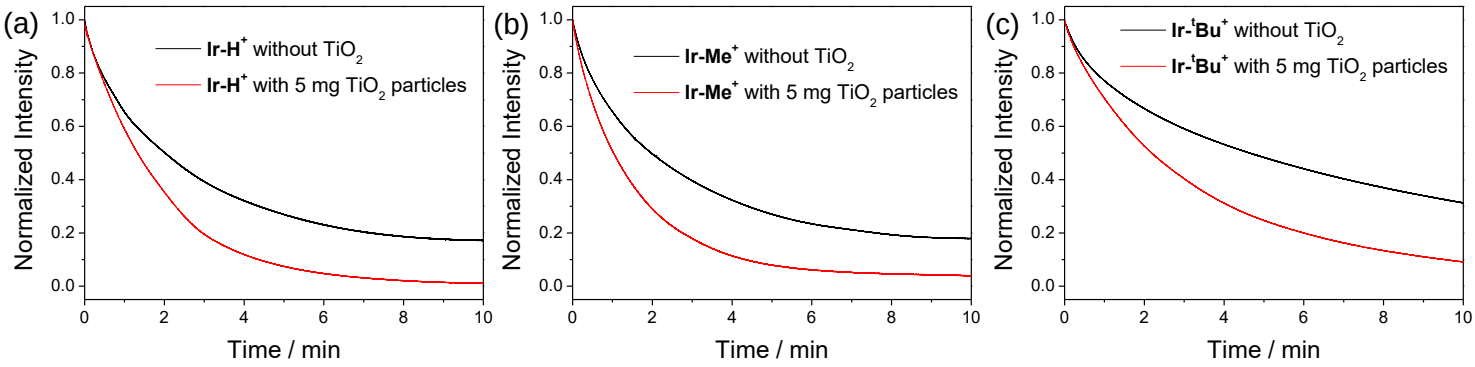

Figure S20. Normalized decay profiles of the absorption at (a) 523 nm (λ_{max} of [**Ir-H**$^+$]$^{-\bullet}$) and (b) 534 nm (λ_{max} of [**Ir-Me**$^+$]$^{-\bullet}$), and (c) 529 nm (λ_{max} of [**Ir-^{t}Bu**$^+$]$^{-\bullet}$) in the dark after 30 s irradiation of 3 mL DMF solution of 25 μM **Ir-X**$^+$, 2.5 mM BIH, and 2.5 vol% H_2O in the absence of TiO_2 (black line), with 5 mg TiO_2 particles placed in the bottom of the cell (red line). Compared to 2 min irradition condition (Figure S19), the relatively fast decay of radical anion absorption in the absence of TiO_2 particles is thought to be due to reduction of the amount of photo-generated radical anion species.

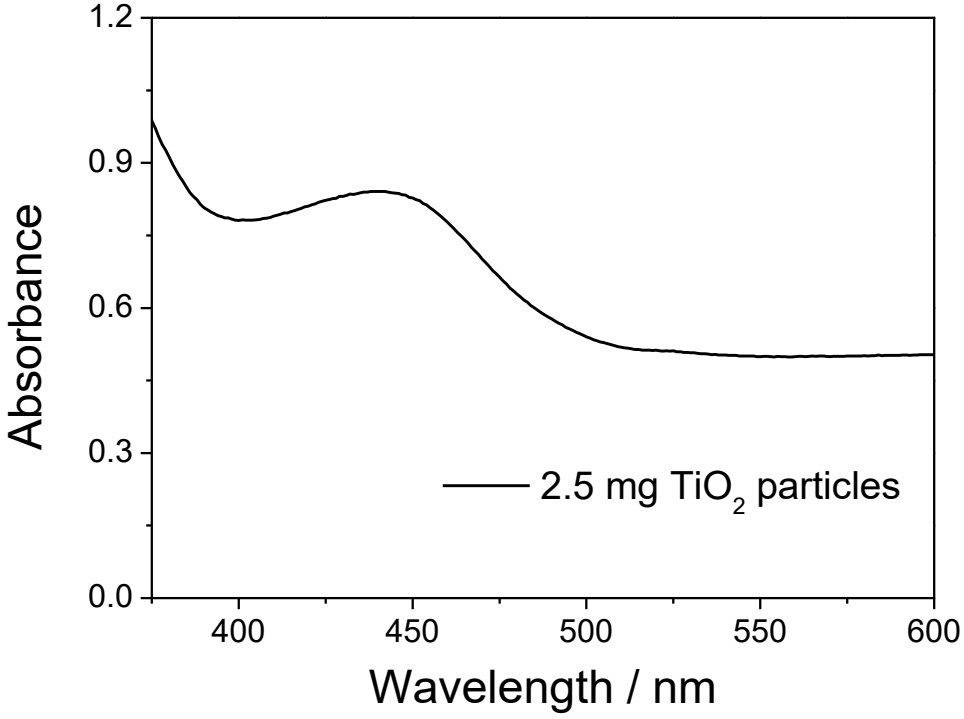

Figure S21. Absorption spectra of 2.5 mg TiO_2-dispersed Ar-saturated DMF/H_2O mixture solvent (2.5 vol% water) containing 0.5 mM **Ir-^{t}Bu$^+$** and 0.25 mM BIH after 1 h irradiation. The added TiO_2 particles were dispersed by stirring during measurement.

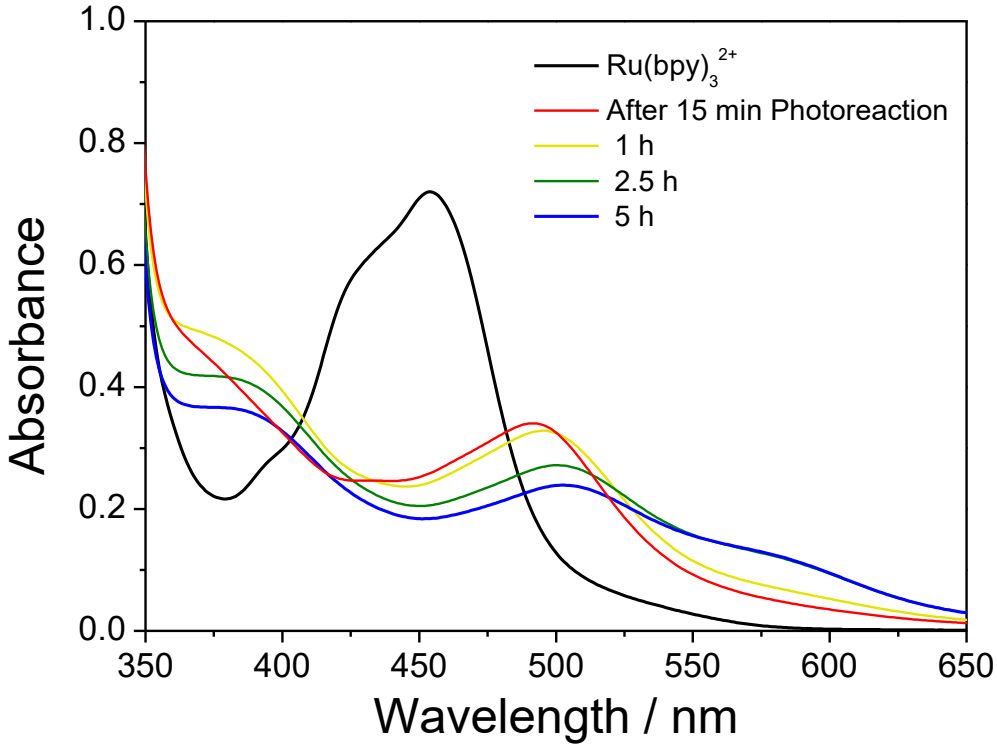

Figure S22. Absorption spectra of $Ru(bpy)_3^{2+}$ before (black line) and after photosensitized CO_2 reduction for 15 min (red line), 1 h (yellow line), 2.5 h (green line), and 5 h (blue line); 3 mL CO_2-saturated DMF/H_2O mixture solvent (2.5 vol% water) containing 1 mM $Ru(bpy)_3^{2+}$, 10 mg TiO_2/ReC (0.1 μmol) particles, and 0.1 M BIH.

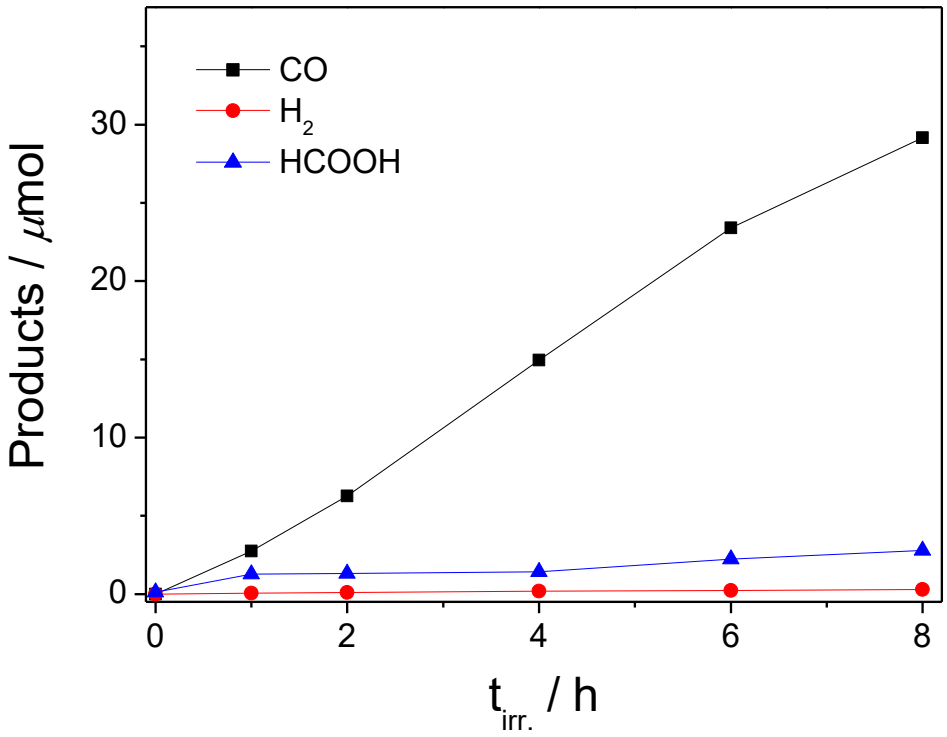

Figure S23. Plot for the formation of CO, H_2, and HCOOH versus irradiation time for dispersion of 10 mg TiO_2/ReC in CO_2-saturated DMF/H_2O mixture solvent (2.5 vol% H_2O) containing 1 mM **Ir-^{t}Bu**$^+$ and 0.1 M BIH; LED irradiation at > 400 nm.

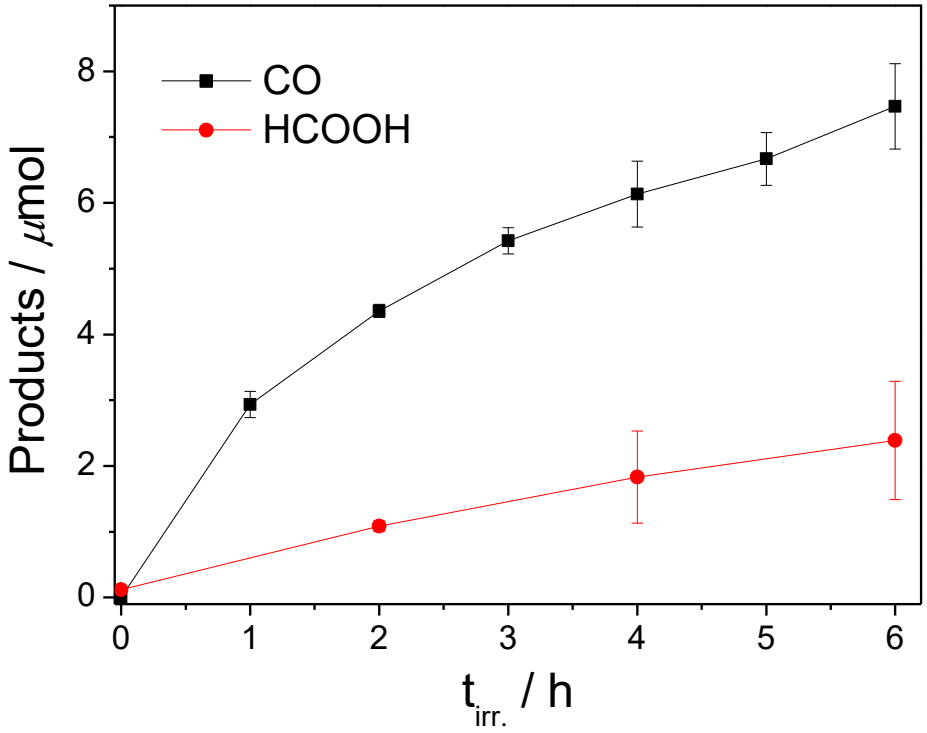

Figure S24. Plots for the formation of CO and HCOOH versus irradiation time for dispersion of 10 mg TiO_2/ReC in CO_2-saturated DMF/H_2O mixture solvent (2.5 vol% H_2O) containing 1 mM $Ru(bpy)_3^{2+}$ and 0.1 M BIH; LED irradiation at >400 nm.

Table S11. Amounts of products and selectivity of CO after 4 h irradiation in photocatalytic CO_2 reduction using the binary **Ir-^{t}Bu$^+$**–TiO_2/ReC catalyst in different conditions.[a]

Entry	Solvent	H_2O / vol%	Atmosphere	Amount of CO produced @4 h / μmol			$HCOOH_{portion}$[b]	CO selectivity[c]
				CO	HCOOH	H_2		
1	DMF	2.5	CO_2	14.94	1.41	0.19	0.08	90
2	DMF	2.5	N_2	*n.d.*[e]	5.44	0.99		
3	DMF	0	N_2	*n.d.*[e]	1.25	0.10		
4	DMA	2.5	CO_2	12.09	0.46	0.11	0.04	95
5[d]	DMF	2.5	CO_2	*n.d.*[e]	*n.d.*[e]	*n.d.*[e]		
6[f]	DMF	2.5	CO_2	0.73	2.05	0.31		
7[f]	DMF	2.5	N_2	*n.d.*[e]	1.90	0.1		

[a]Reaction conditions: 1 mM **Ir-^{t}Bu$^+$** + 10 mg TiO_2/ReC in the presence of 0.1 M BIH. [b]The portion of HCOOH in mixed gas production is obtained from the following equation: $HCOOH_{portion}$ = HCOOH / (CO + HCOOH + H_2). [c]The CO selectivity is obtained from the following equation: CO selectivity = (CO / (CO + HCOOH + H_2)) × 100. [d]Dark condition. [e]Not detected. [f]In the absence of TiO_2/ReC particles.

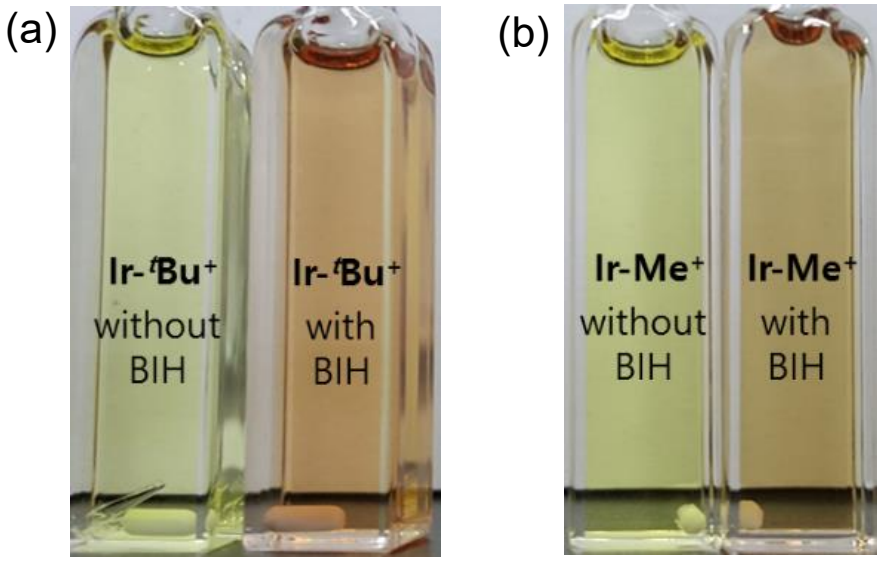

Figure S25. Color change of DMF solutions containing 0.05 mM **Ir-^{t}Bu$^+$** (a) and **Ir-Me$^+$** (b) in the absence (left) and in the presence (right) of 0.25 mM BIH under LED irradiation.

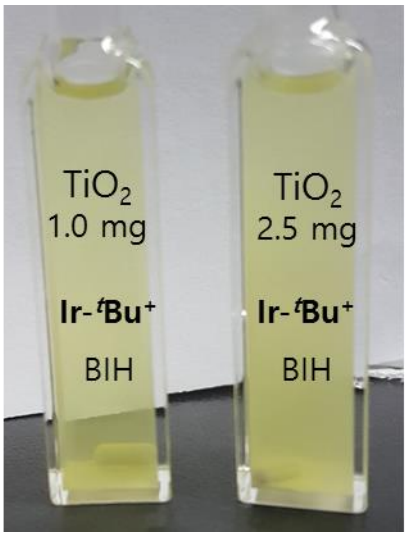

Figure S26. Suspensions of 1 mg (left) and 2.5 mg (right) TiO_2 particles in Ar-saturated DMF containing 0.05 mM **Ir-^{t}Bu$^+$** and 0.25 mM BIH after 1 h stirring under LED irradiation.